Journal of Alloys and Compounds 948 (2023) 169552

Contents lists available at ScienceDirect

Journal of Alloys and Compounds

journal homepage: www.elsevier.com/locate/jalcom

# Spark plasma sintering and optical properties of $Tm^{3+}$ and $Tm^{3+}$ /$Yb^{3+}$ doped $NaLaF_4$ transparent glass-ceramics

M. Sedano [a], S. Babu [b], R. Balda [c,d], J. Fernández [e], A. Durán [a], M.J. Pascual [a,*]

[a] Instituto de Cerámica y Vidrio (ICV-CSIC), 28049 Madrid, Spain
[b] Dept. of Coating Processes, FunGlass, Alexander Dubček University of Trenčín, Študentská 2, 911 50 Trenčín, Slovakia
[c] Dept. Física Aplicada, Escuela Superior de Ingeniería, Universidad del País Vasco (UPV-EHU), 48013 Bilbao, Spain
[d] Centro de Física de Materiales, (CSIC-UPV/EHU), 20018 San Sebastian, Spain
[e] Donostia International Physics Center (DIPC) 20018 San Sebastian, Spain

ARTICLE INFO

*Article history:*
Received 18 July 2022
Received in revised form 3 February 2023
Accepted 4 March 2023
Available online 6 March 2023

*Keywords:*
Transparent glass-ceramics
$NaLaF_4$
Spark plasma sintering
Oxyfluoride glass-ceramics
$Tm^{3+}$ ions

ABSTRACT

$Tm^{3+}$ doped oxyfluoride glass-ceramics (GCs) containing $NaLaF_4$ nanocrystals (NCs) have been obtained by spark plasma sintering (SPS). First, the precursor glasses were melted and then milled and sieved to a suitable particle size. Glass powder pellets were sintered by spark plasma sintering under vacuum conditions. The SPS processing parameters (temperature, pressure, and holding time) were optimized to obtain transparent glass-ceramics. The times of SPS processing are considerably shorter compared with those for the preparation of these GCs by conventional thermal treatment. All glass-ceramics contain nanocrystals of the β- $NaLaF_4$ phase with an average crystal size of 20 nm, but the more highly doped samples ($2Tm^{3+}$ and $0.5Tm^{3+}/2Yb^{3+}$) show evidence of the presence of another phase corresponding with α-$NaLaF_4$. The luminescence properties of the near infrared (NIR) emissions of $Tm^{3+}$ for different concentrations reveal the presence of concentration quenching of the $^3H_4$ and $^3F_4$ levels. The analysis of the decay from the $^3H_4$ level with increasing concentration is consistent with a dipole-dipole quenching process assisted by energy migration, whereas the self-quenching of the $^3F_4 \rightarrow {}^3H_6$ emission can be attributed to fast diffusion. Energy transfer between $Yb^{3+}$ and $Tm^{3+}$ ions is confirmed by the NIR and up-converted (UC) emissions after $Yb^{3+}$ excitation at 975 nm. No UC emission is observed under 791 nm excitation of $Tm^{3+}$ ions.



## 1. Introduction

Rare earth (RE) doped transparent oxyfluoride GCs have been demonstrated to be promising materials for applications in different fields such as solid- state lasers, down- and up- conversion phosphors or optical amplifiers [1]. The major advantage of these materials is the combination of the mechanical and chemical properties of the oxide glasses with the low phonon energy (300 – 500 $cm^{-1}$) of fluoride crystals. Fluoride nanocrystals, produced after controlled heat treatment of the glass, are excellent hosts for the RE ions [2–5].

GCs can be prepared by the conventional method which implicates using prolonged heat treatments (more than 10 h) in order to obtain the desired NCs [6–8]. These long heat treatments are necessary to get strict control of the nucleation and crystal growth processes and to achieve transparency in these GCs. Crystals must be on the nanometric scale (below 40 nm) in order to avoid light scattering [4,9,10]. In recent years, the SPS method is gaining interest in the preparation of transparent GCs from sintering and crystallization of the corresponding glass powders. There are different works reporting transparent glass-ceramics of different classes processed by SPS. As an example, tellurium- based GCs were prepared combining the melt-quenching method with SPS. The authors observed that the densification through the viscous sintering of the glass occur at lower temperatures (463 K) compared with the pure system (700 K) [11]. Other example is the processing of chalcogenide glasses [12]. In this work, the authors used protective tantalum foils to avoid the carbon diffusion. They prepared milled glass powder at different times (0–80 h) and they observed changed color of the glass powder, from gray to red. The SPS sintering was performed using different dwelling times (2–60 min) at 390 °C.

In relation to transparent oxyfluoride glass-ceramics, hardly any work can be found in the literature on this type of GCs. There are only a couple of papers involving the crystalline phases of $LaF_3$ [13] and $KLaF_4$ [14]. Huang et al. [13] prepared $LaF_3$ nanoparticles by sol-gel, and then disperse them in a silica powder. The bulk material was

* Corresponding author.
*E-mail address:* mpascual@icv.csic.es (M.J. Pascual).

https://doi.org/10.1016/j.jallcom.2023.169552

obtained by SPS after treatment at 950º for 1 min. The $LaF_3$ crystals size was less than 50 nm.

The SPS method has the advantages of simultaneous complete densification and crystallization of the fluoride NCs during a fast heating rate and very short holding times at the treatment temperature. Additionally, improved mechanical properties can be achieved [15,16]. This method combines temperature, pressure, and electric field to generate spark plasma. This process allows the desired crystalline phase to be obtained, controlling the NC size, reducing grain boundaries and porosity, for which the optimization of the processing parameters (particle size, temperature, pressure, and holding time) is crucial. Nevertheless, carbon contamination coming from graphite punch is still an issue, different authors [17–19] have suggested as possible solutions pre-compacting the powder (making a pellet), applying a pre-sintering treatment, and using protective foils of tantalum, molybdenum, alumina or platinum.

GCs with different crystalline phases such as $LaF_3$ [20,21], $KLaF_4$ [22,23], $NaLaF_4$ [24,25], $NaLuF_4$ [26,27], $NaGdF_4$ [28,29] and $NaYF_4$ [30,31] have been prepared and studied previously using the conventional heat treatment method. In every situation, luminescence properties improve in GCs compared to the precursor glass due to the presence of a crystalline phase doped with RE ions.

In previous work, the crystallization of $KLaF_4$ nanocrystals was achieved using the SPS method [14]. The sintering parameters: temperature, pressure, holding time and particle size of the glass powder were optimized in order to obtain samples with good optical transparency. It was observed that the use of large particle sizes, 100-63 µm, favored the transparency. Nevertheless, one of the major drawbacks of the SPS technique was carbon contamination from the graphite dies and punches used. The use of large particle sizes together with platinum protective films reduced this type of contamination. Structural and optical characterization confirmed the presence of the α-$KLaF_4$ phase as the major phase, as well as the presence of the dopant in both the crystalline and amorphous phases. The methodology used to obtain transparent glass-ceramics samples by SPS showed in that work, could be applied to other crystalline systems.

In particular, the $NaLaF_4$ crystal phase with hexagonal symmetry presents a low phonon energy ($E_{ph}$ = 290 $cm^{-1}$), which makes this phase a promising material for up- conversion (UC) luminescence application and host material for RE ions. GCs containing this double fluoride phase have been prepared by conventional thermal treatment and have been reported in [32,33]. The base glass doped with 0.7 mol%. of $Tm_2O_3$ and heat treated between 540 and 580 ℃ for more than 20 h led to the crystallization of β- $NaLaF_4$. The crystal size varied between 12 and 16 nm. The location of $Tm^{3+}$ inside the crystal phase was confirmed by photoluminescence measurements. Additionally, thulium is a very interesting RE dopant for its near infrared emissions for optical amplification applications and blue UC emission from the excitation in the near infrared range [34].

In the present study, GCs with crystalline phase $NaLaF_4$ doped with $TmF_3$ and codoped with $YbF_3$ in different amounts have been prepared by SPS, and their structural and optical properties characterized and compared with GCs prepared by the conventional thermal treatment method previously reported in our research group [33]. The spectroscopic properties of the near infrared and up-converted emissions of $Tm^{3+}$ ions have been characterized by using steady-state and time-resolved laser spectroscopy. The study includes absorption and emission spectra and lifetime measurements for the $Tm^{3+}$ infrared fluorescence. The energy transfer between $Yb^{3+}$ and $Tm^{3+}$ ions is confirmed by the NIR and UC emissions after $Yb^{3+}$ excitation at 975 nm. Back transfer from $Tm^{3+}$ to $Yb^{3+}$ is present under near-infrared excitation of $Tm^{3+}$ ions at 791 nm. The possible up-conversion processes leading to the population of several excited levels are discussed.

## 2. Experimental procedure

Glasses with composition 70$SiO_2$- 7$Al_2O_3$- 8 $K_2O$- 8$Na_2O$- 7$LaF_3$ (mol%.) doped with 0.1, 0.5, 1, and 2 mol%. $TmF_3$; and samples doped with 0.5 $TmF_3$ and co-doped with 1 and 2 mol%. $YbF_3$, were prepared as previously described in [33]. The only change is the raw materials used to introduce the $Tm^{3+}$ ions. In the previous works, $Tm_2O_3$ was the raw material.

All doped glasses were milled and sieved in order to obtain powder fractions of <63 µm and 100-63 µm. Previous studies with $KLaF_4$ crystalline phase [14], have shown that particle sizes between 100 and 63 µm provide samples with higher transparency. The samples were ground in an agate jar along with agate balls using a planetary mill at 250 rpm for 15 min. The powder obtained was sieved in order to get the desired particle size fractions. The particle size distribution of the glass powders was measured with a Mastersizer 3000 using the Fraunhofer approach. The average particle size for the small fraction was 27 µm, while for the large fraction was 91 µm.

The glass powder was weighed to prepare pellets with 15 mm diameter and 5 mm thickness. The pellets were pressed under 94 MPa for 5 min using a hydraulic press, and they were pretreated at 450 ℃ for 30 min in order to promote some compaction.

The SPS experiments were carried out with an SPS- 510 CE equipment (Fuji Electronic Industrial Co., Ldt), in a vacuum atmosphere using the pressure of 22 MPa. The temperature of 610 ℃ was kept for 20 min holding time. Pulsed direct current (pulses of 12 ms ON/2 ms OFF) was applied. The sintering temperature ($T_s$) was controlled by a thermocouple inserted into the graphite die wall. In order to avoid carbon contamination from the die, samples were covered with platinum foil. The samples obtained showed signs of carbon contamination despite the precautions taken, so the samples were ground. The samples for optical characterization were polished using SiC paper with decreasing grain size (P1200, P2500, and P4000) and diamond suspension with decreasing particle sizes 6, 3, and 1 µm.

The density of precursor glasses and the corresponding GCs was measured using Archimedes' method.

### 2.1. Thermal characterization of the precursor glass

Hot-stage microscopy (HSM) of the precursor glass powders was performed in order to determine the sintering range and an optimum treatment temperature for the SPS experiments. A Leica – EM201 microscope was used at a heating rate of 10 °C/min up to 1200 °C. Glass powder with particle size <63 µm was cold pressed to form samples with 3 mm in both height and diameter.

### 2.2. Structural characterization

X- ray diffraction (XRD) was used to characterize the GC samples using a Bruker D8 AXE diffractometer (CuKα = 1.5406Å). Acquisition parameters were angular range $10 \leq 2\theta \leq 70°$ in a step size of 0.02° and fixed counter time of 1 s per step. The XRD patterns were determined by Diffrac.EVA software using PDF as a crystallography base. The crystallization peak at 2θ around 28.6° was used for the estimation of the crystal size using the Scherer equation as previously described in [33].

The same GCs powders, dispersed in ethanol, were studied by high resolution transmission electron microscopy (HR- TEM) with a TEM/ STEM JEOL 2100 F equipment working at 200 kV with a point of resolution of 0.19 nm. Micrograph analysis was carried out using ImageJ® software.

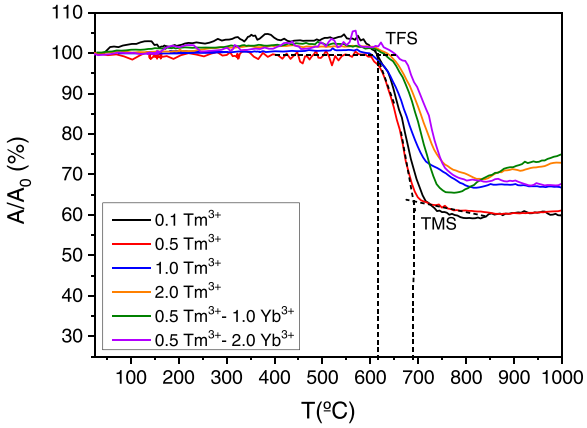


**Fig. 1.** Variation of the sample area as a function of temperature for different dopant concentration. The particle size of glass powder is <63 µm.

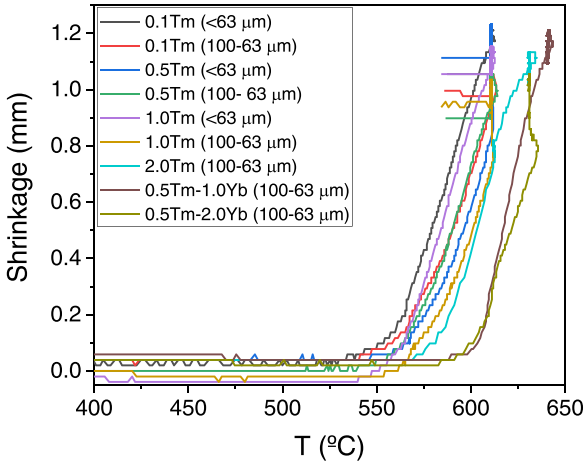


**Fig. 2.** Shrinkage curves as a function of temperature recorded in situ during the SPS experiment.

### 2.3. Optical characterization

Conventional absorption and transmission spectra were performed with a Cary 5000 spectrophotometer. The steady-state emission measurements were made with a Ti-sapphire ring laser (0.4 $cm^{-1}$ linewidth) as exciting light. The fluorescence was analyzed with a 0.25 monochromator, and the signal was detected by an extended IR Hamamatsu H10330A-75 photomultiplier and finally amplified by a standard lock-in technique. Up-converted emission was detected by a Hamamatsu R636 photomultiplier.

The decay times were obtained by exciting the samples with a Ti: sapphire laser pumped by a pulsed, frequency-double Nd: YAG laser (9 ns pulse width), and detecting the emission with an extended IR Hamamatsu H10330A-75 photomultiplier. The photomultiplier output was recorded by using a Tektronix oscilloscope. All measurements were performed at room temperature.

## 3. Results and discussion

### 3.1. Thermal characterization of the precursor glasses

Fig. 1 shows the variation of the sample area as a function of temperature for all the studied compositions. $A/A_0$ is the area of the sample divided by the initial area expressed as a percentage. As an example, the estimation of the temperature of first shrinkage ($T_{FS}$) and maximum shrinkage ($T_{MS}$) are shown for the composition of $0.5Tm^{3+}$. The estimation of these two temperatures is done by means of tangent lines to the curve, as shown in the figure. The $T_{FS}$ range was 604–633 (±10 °C) considering all samples and the $T_{MS}$ range 700–760 (±10 °C). The $T_{FS}$ increases as the amount of dopant and co-dopant increases. In order to perform the SPS experiments, a temperature within the $T_{FS}$ range (610 °C) was selected except for 2.0Tm, 0.5Tm- 1.0Yb and 0.5Tm- 2.0Yb compositions that needed some higher sintering temperature (630 °C).

Fig. 2 shows the shrinkage as a function of the temperature measured in situ during the SPS experiment. The first measurable shrinkage is around 560 ℃ and increased up to 610 ℃. The shrinkage between 560 and 610 ℃ is likely originated from viscous flow sintering at temperatures close to the glass transition temperatures ($T_g$). The $T_g$ for these compositions is between 505 and 542 ℃, studied in [32,33]. During the isothermal holding time at 610 ℃ (20 min), densification, transparency, and crystallization of the desired phase occur. The temperature selected from the HSM study appears to be optimal for fixing the parameters of the SPS process.

For the sintering of the $2Tm^{3+}$ and $0.5Tm^{3+}$ samples co-doped with $1Yb^{3+}$ and $2Yb^{3+}$, a temperature of 630 °C was required. This is due to the fact that the increase in the amount of Tm or the introduction of Yb as a co-dopant increases glass viscosity [35–37].

### 3.2. GCs obtained by SPS

Well- densified samples, with a cylindrical shape, were obtained. The diameter was kept to 15 mm and the thickness decreased from the initial 5 mm to around 3 mm. SPS presents a great inconvenience, carbon contamination which comes from the graphite die and graphite foil barrier between samples and punches, causing the sample to darken and even turn black. Covering the die with platinum foil helps to reduce this type of contamination as described in [19].

As an example, Fig. 3 shows the picture of GC samples obtained after the SPS experiment. All samples are optically transparent and

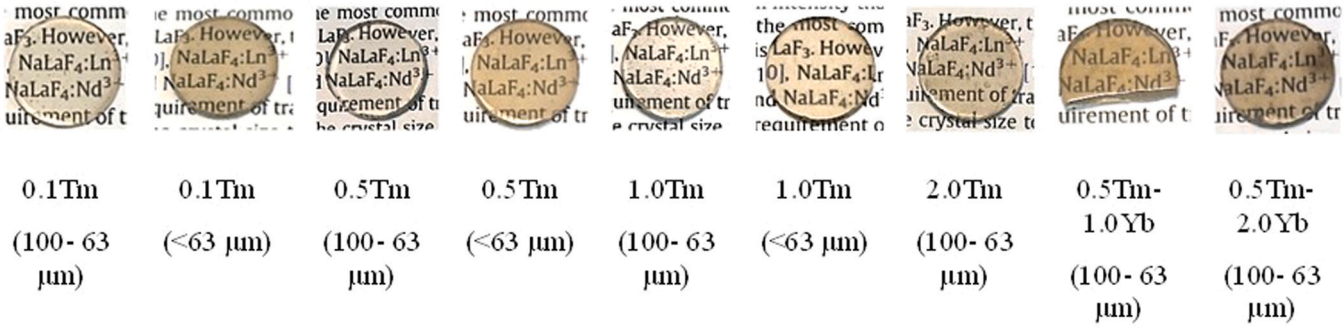


**Fig. 3.** $NaLaF_4$ SPS GCs doped with different amounts of $TmF_3$ and co-doped with 1.0 and 2.0 mol% of $YbF_3$ processed at 630 ℃, 20 min, 22 MPa.

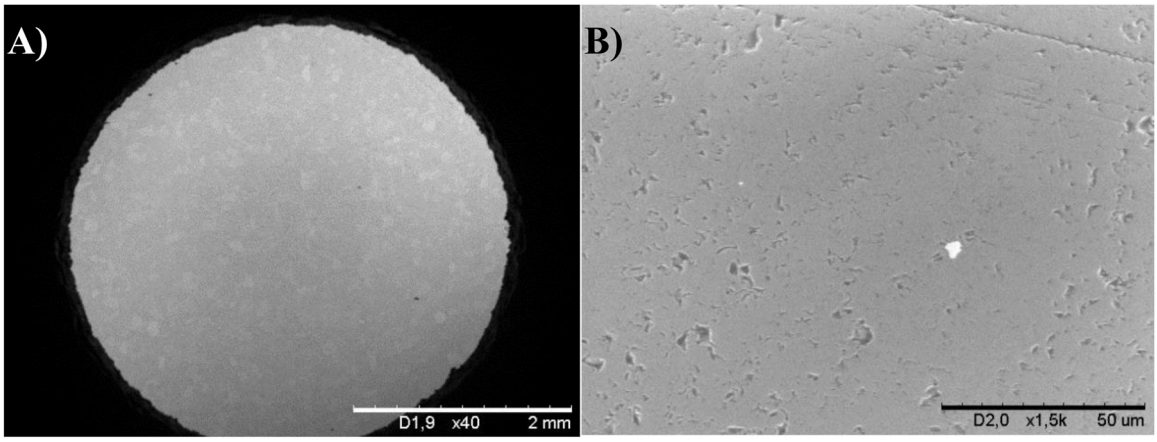


**Fig. 4.** a) and b) SEM images of $NaLaF_4$: 0.5$Tm^{3+}$ SPS GCs (100–63 μm) at different magnifications.

**Table 1**
Densities (g/cm$^3$) ± 0.01 for the base glasses and SPS-GCs.

| Sample | Base glass | SPS-GCs |
|---|---|---|
| 0.1 $Tm^{3+}$ | 2.67 | 2.68 |
| 0.5 $Tm^{3+}$ | 2.68 | 2.69 |
| 1.0 $Tm^{3+}$ | 2.70 | 2.71 |
| 2.0 $Tm^{3+}$ | 2.73 | 2.77 |
| 0.5 $Tm^{3+}$- 1 $Yb^{3+}$ | 2.71 | 2.74 |
| 0.5 $Tm^{3+}$- 2 $Yb^{3+}$ | 2.75 | 2.79 |

light scattering have not been observed which indicated that they are highly homogeneous.

In a previous work [14], it was explained how carbon contamination occurs in the samples. Basically, during the viscous sintering stage, CO is deposited in the pores of the sample. As sintering occurs the gas trapped in the pores dissolves leaving the carbon deposited. This carbon deposition can be described by the following exothermic reaction 2CO (g) = $CO_2$ (g) + C (s) [38]. Fig. 4a and b show images for sample doped with 0.5 $Tm^{3+}$ (100–63 μm) at different magnifications, where is possible to see this issue.

Table 1 shows the density values for the base glass and the GC samples. As can be seen, the densities are very similar which means that the densification of SPS GCs has been completed, although the density for SPS GCs samples is low. The density of the $NaLaF_4$ phase (4.7 g·cm$^{-3}$) is higher, and the densities of the SPS GCs samples should be higher than the corresponding base glass. In this work, the amount of crystalline fraction was not determined but it was analysed for undoped $NaLaF_4$ GCs obtained by heat treatment [32]. This amount is rather low (~ 5.2 wt%). Also, the presence of porosity in GCs samples (Fig. 4(b)) can reduce the density of these samples.

### 3.3. Structural characterization

Fig. 5(a) and (b) show the X-ray diffraction (XRD) patterns for the samples obtained by SPS sintered at 610 °C for 20 min for different particle sizes of the glass powder. $NaLaF_4$ with hexagonal symmetry (JCPDS 075 1923) is the only crystalline phase being detected for samples doped from 0.1 to 1 mol%. $TmF_3$ and the codoped 0.5 $Tm^{3+}$-1$Yb^{3+}$. This phase corresponds with the beta polymorph. For samples 0.5$Tm^{3+}$-2$Yb^{3+}$ and 2$Tm^{3+}$, $NaLaF_4$ is the main crystalline phase but it crystallizes together with $LaF_2$ crystalline phase (JCPDS 033 0704) with face centered cubic symmetry. $La^{2+}$ ions, are impossible to obtain at the melting temperatures used. Y. Peng et al. [39] observed that in their samples they also obtained this phase and concluded that actually the phase obtained is α-$NaLaF_4$ instead of $LaF_2$. The XRD results confirm the presence of the desired crystalline phase, β-$NaLaF_4$, in the SPS samples.

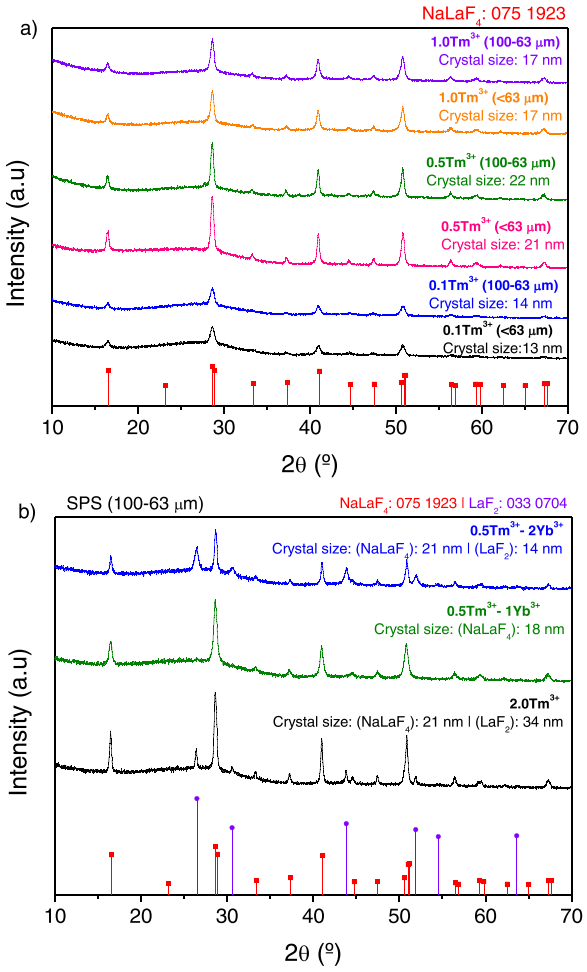


**Fig. 5.** (a) XRD patterns obtained for SPS GCs from different powder particle sizes and doped between 0.1 and 1.0 $Tm^{3+}$, (b) XRD patterns for SPS GCs doped with 2.0$Tm^{3+}$ and 0.5$Tm^{3+}$ co-doped with 1.0$Yb^{3+}$ and 2.0$Yb^{3+}$. Crystal sizes have been included.

The crystal sizes can be seen in Fig. 5(a) and (b). These results are similar to those obtained for conventional heat treatment glass-ceramics [33]. Moreover, no significant differences with respect to crystal size for samples with different particle sizes are observed.

To complete the structural analysis, all samples were studied by HR-TEM and related selected area electron diffraction (SAED). Figs. 6 and 7 show, as an example, micrographs obtained of SPS GCs doped with 0.5 $Tm^{3+}$ and codoped with 1$Yb^{3+}$ and 2$Yb^{3+}$.

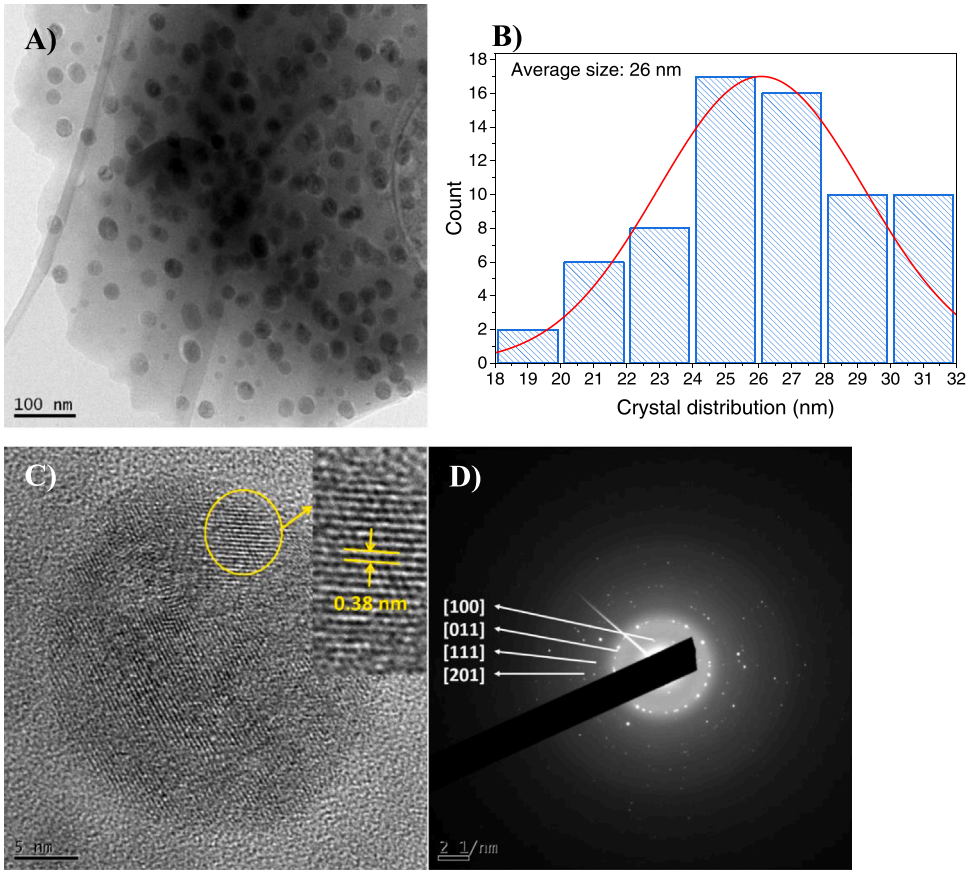


**Fig. 6.** (a) TEM micrographs of SPS GCs 0.5$Tm^{3+}$ (100–63 µm, 20 min), (b) crystal size distribution, (c) details of a β- $NaLaF_4$ nanocrystal and (d) electron diffraction pattern.

Fig. 6(a) shows a micrograph of nanocrystals showing two different crystal sizes, although it is not possible to measure the smaller ones. Fig. 6(b) shows the distribution of crystal size, the average size is 26 nm. This result is in agreement with that obtained by XRD (22 nm). The D-space was 0.38 nm which corresponds to the [001] of β- $NaLaF_4$ (Fig. 6(c)). Fig. 6(d) is the SAED pattern with the corresponding planes for this crystalline phase.

Finally, in Fig. 7(b) is possible to show the crystal size distribution, where the average size was 19 nm in accordance with the XRD result (21 nm). Although two different crystalline patterns where observed by XRD, it was not possible to distinguish other crystal distributions by TEM. Fig. 7(c) shows 0.38 nm as D-space corresponding with the [001] plane of β- $NaLaF_4$ crystalline phase. Fig. 7(d) shows the SAED patterns together with the planes corresponding with β- $NaLaF_4$ phase.

In previous work [32], GC samples obtained by conventional heat treatment showed the existence of damaged regions in areas close to the crystals. These regions are enriched in Si, which provide a diffusion barrier avoiding crystal growth and allowing uniformity in the crystal size. The maximum treatment temperature for these samples was 625 ºC, although at this temperature the samples started to become opalescent. While for the samples obtained by SPS, the temperatures were between 610 and 630 ºC, the appearance of the samples was practically transparent. Moreover, this increase in temperature increases the size of the crystals, from 20 nm for the samples obtained by conventional treatment to almost 30 nm for the samples obtained by SPS.

### 3.4. Optical properties

The room temperature absorption spectra were recorded for the more transparent samples (0.1, 0.5, 1 mol%. $TmF_3$ and 0.5 mol%. $TmF_3$-2 mol%. $YbF_3$) in the 350–2000 nm spectral range. As an example, Fig. 8 shows the absorption coefficient as a function of wavelength for the GC samples doped with 0.5 $TmF_3$ and codoped with 0.5$TmF_3$-2$YbF_3$ (in mol%) prepared with a particle size between 100 and 63 µm. The spectra show the bands corresponding to the transitions starting from the $^3H_6$ ground state to the different higher levels $^1G_4$, $^3F_2$, $^3F_3$, $^3H_4$, $^3H_5$, and $^3F_4$ of $Tm^{3+}$. In addition to the $Tm^{3+}$ absorption bands, the spectrum of the codoped sample shows the intense band at 975 nm corresponding to the $^2F_{7/2} \rightarrow {}^2F_{5/2}$ transition of $Yb^{3+}$. The spectra obtained for the single doped samples doped with 0.1 and 1 mol%. $TmF_3$ are similar, except for the band intensities. The spectrum of the codoped sample shows a higher background absorption and a red-shift of the absorption edge, probably due to some carbon contamination.

The transmission spectra were performed for all samples in the 350–2000 nm range. Fig. 9(a) shows, as an example, the spectra as a function of wavelength for SPS- GCs doped with 1 mol%. $TmF_3$ prepared with a glass powder particle size < 63 µm and 100–63 µm. The spectra show the bands corresponding to the transitions starting from $^3H_6$ ground state to the different higher energy levels of $Tm^{3+}$ ions. As can be seen, the sample prepared with particle size 100–63 µm is more transparent with a transmittance of 78 %. On the other hand, Fig. 9(b) shows the transmission spectra for samples doped 0.5 mol%. $Tm^{3+}$ and co-doped with 2.0 mol%. $Yb^{3+}$. As for the previous samples, the spectra show the bands corresponding to the transitions of the $Tm^{3+}$ ions, and in the case of the sample co-doped with $Yb^{3+}$, the presence of the band corresponding to the $^2F_{7/2} \rightarrow {}^2F_{5/2}$ transition of the $Yb^{3+}$ ions at 975 nm is observed.

The near-infrared emission of the single doped samples with 0.1, 0.5, and 1 mol% $TmF_3$ was obtained at room temperature in the 1250–1700 nm spectral range by exciting at 791 nm in resonance with the $^3H_4$ ($Tm^{3+}$) level. As an example, Fig. 10 shows the

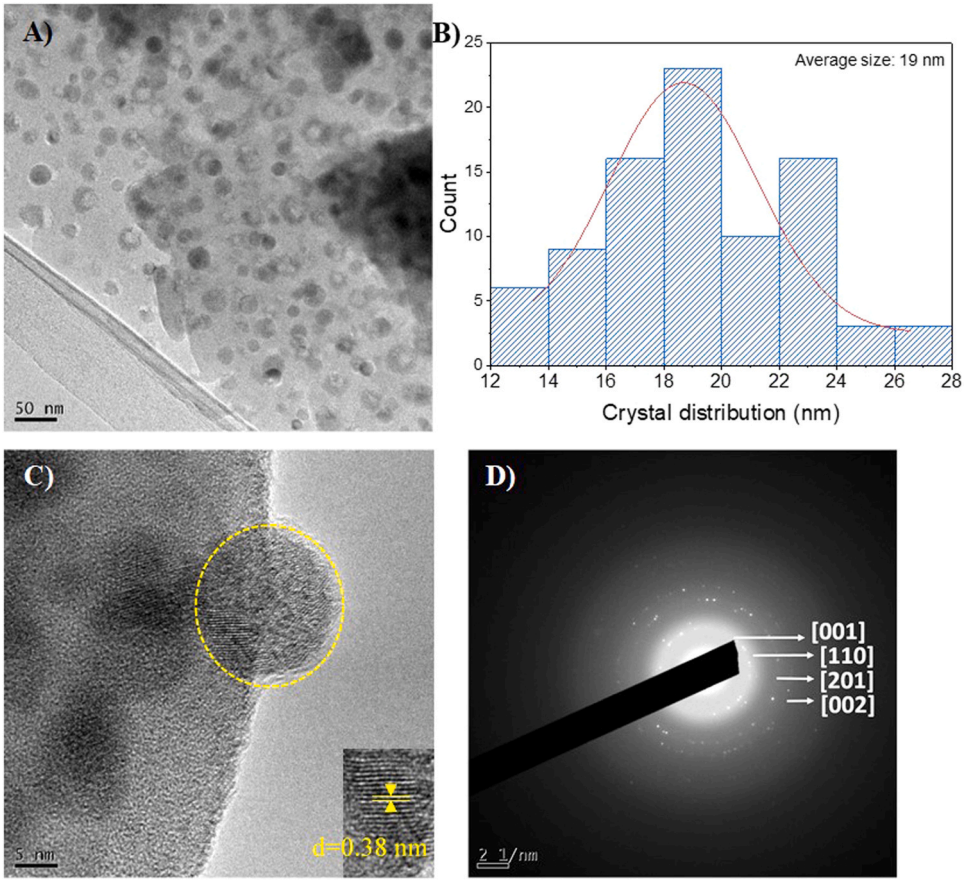


**Fig. 7.** (a) TEM micrographs of SPS GCs 0.5$Tm^{3+}$- 2.0$Yb^{3+}$ (100–63 µm, 20 min), (b) crystal size distribution, (c) details of a β- $NaLaF_4$ nanocrystal and (d) electron diffraction pattern.

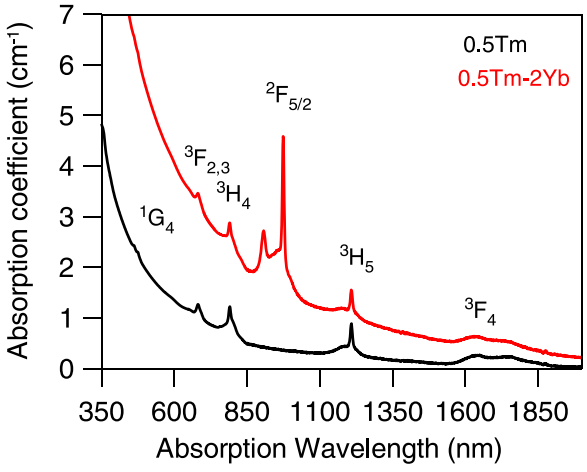


**Fig. 8.** Room temperature absorption coefficient for glass-ceramic (GC) samples doped with 0.5 mol% $Tm^{3+}$ (black) and codoped with 0.5 mol%. $Tm^{3+}$-2 mol%. $Yb^{3+}$ prepared with particle size between 100 and 63 µm.

fluorescence spectra corresponding to the GCs samples doped with 0.5 mol% $Tm^{3+}$ prepared with a particle size < 63 µm and 100–63 µm. The spectrum of the glass samples is also included for comparison. The spectra show the emission band corresponding to the $^3H_4 \rightarrow {}^3F_4$ transition with a maximum of around 1450 nm together with the high energy component of the $^3F_4 \rightarrow {}^3H_6$ transition around 1650 nm. The long-wavelength part of the $^3F_4 \rightarrow {}^3H_6$ emission is not observed due to the upper limit of the detector. The $^3H_4 \rightarrow {}^3F_4$ transition of the GCs shows at least five Stark components which suggests a crystalline environment for $Tm^{3+}$ ions. In the case of the glass sample, the spectrum is less resolved with lower intensity. The samples prepared with particle size 100–63 µm present higher intensity than those prepared with particle size < 63 µm for all $TmF_3$ concentrations. Similar emission spectra are obtained for the three $TmF_3$ concentrations corresponding to the highest intensity to the 1 mol%.

The codoped sample with 0.5 mol%. $TmF_3$ and 2 mol%. $YbF_3$ was excited at 791 nm ($Tm^{3+}$) where only $Tm^{3+}$ ions absorb and at 975 nm ($Yb^{3+}$), the maximum absorption of $Yb^{3+}$, to analyze the energy transfer between both ions. The NIR emission spectra of the codoped sample for both excitation wavelengths are presented in Fig. 11. The presence of the $^2F_{5/2} \rightarrow {}^2F_{7/2}$ emission of $Yb^{3+}$ ions after excitation of $Tm^{3+}$ ions at 791 nm (Fig. 11(a)) indicates that energy transfer processes from $Tm^{3+}$ to $Yb^{3+}$ occur. After excitation of the $^3H_4$ level of $Tm^{3+}$, the most probable energy transfer mechanism from $Tm^{3+}$ to $Yb^{3+}$ ions is a phonon-assisted energy transfer process: $^3H_4$ ($Tm^{3+}$)→ $^3H_6$ ($Tm^{3+}$): $^2F_{7/2}$ ($Yb^{3+}$) →$F_{5/2}$ ($Yb^{3+}$). The emission spectrum of the single- doped sample is included for comparison. Excitation of $Yb^{3+}$ ions at 975 nm (Fig. 11 (b)) shows the $Yb^{3+}$ emission together with a weak band corresponding to the $^3F_4 \rightarrow {}^3H_6$ transition of $Tm^{3+}$ ions. The short wavelength side of the $^2F_{5/2} \rightarrow {}^2F_{7/2}$ emission is cut by the filter used to avoid the excitation light. This result evidences the Yb-Tm energy transfer.

The lifetime values of the $^3H_4$ and $^3F_4$ emitting levels were obtained for different $Tm^{3+}$ concentrations (0.1, 0.5, and 1 mol%) by

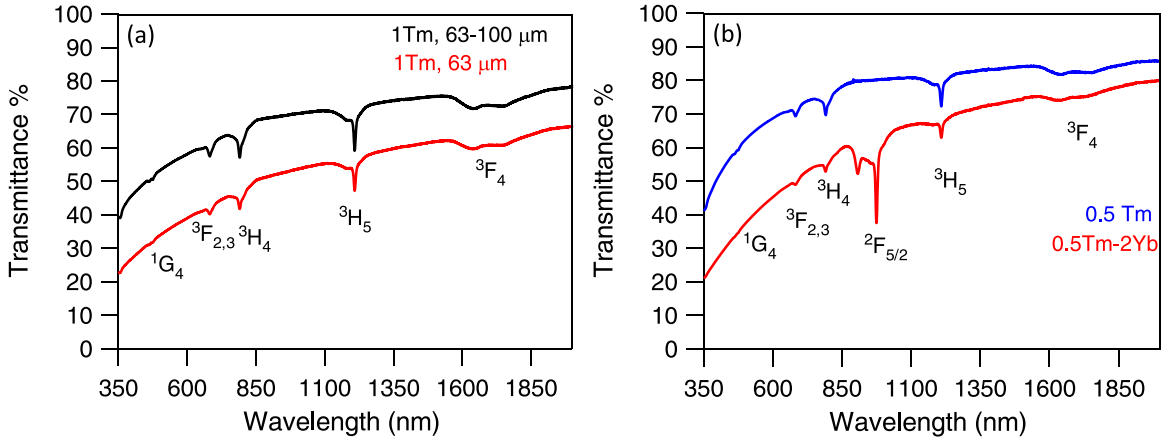


**Fig. 9.** Transmission spectra for (a) SPS-GCs doped with 1.0 mol% Tm prepared with particle size < 63 μm and 100–63 μm and (b) SPS GCS doped with 0.5 mol%. Tm and co-doped 2.0 mol%. Yb prepared with particle size 100–63 μm.

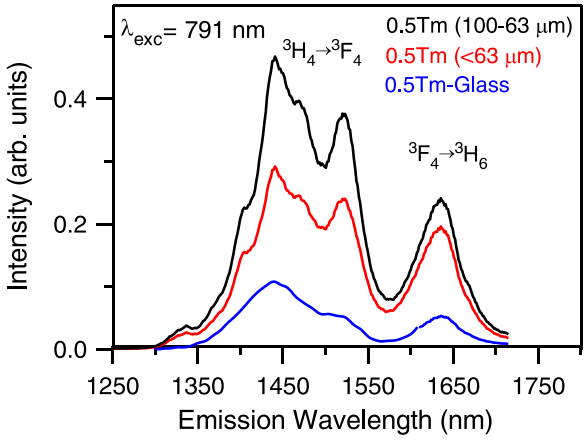


**Fig. 10.** Room temperature emission spectra of $Tm^{3+}$ ions for glass-ceramic (GC) samples doped with 0.5 mol%. $Tm^{3+}$ prepared with particle size < 63 μm (red line) and 100–63 μm (black line), and for the glass sample (blue line).

exciting at 791 nm. Fig. 12(a) shows the semilogarithmic plot of the experimental decays of the $^3H_4$ level for the single-doped samples with 0.1, 0.5, and 1 mol%. $TmF_3$ prepared with particle size between 100 and 63 μm. Similar decays are obtained for the samples prepared with particle size < 63 μm. As can be seen, the decays deviate from a single exponential function, even at low concentrations and the lifetime decreases from 61 μs to 36 μs as $TmF_3$ concentration increases from 0.1 to 1 mol%, which indicates the presence of non-radiative energy transfer processes. The lifetime values in Fig. 12(a) correspond to the average lifetime defined by

$$\langle \tau \rangle = \frac{\int_0^\infty tI(t)dt}{\int_0^\infty I(t)dt} \quad (1)$$

where I (t) represents the luminescence intensity at time t corrected for the background.

The shortening of the lifetimes and the deviation from a single exponential function are characteristics of the existence of a concentration quenching mechanism as concentration increases. This concentration quenching has been previously observed in $Tm^{3+}$-doped systems and attributed to cross-relaxation between $Tm^{3+}$ ions [40]. In this process part of the energy of an ion in the $^3H_4$ level is transferred to another ion in the ground state ending both ions in the $^3F_4$ level ($^3H_4$, $^3H_6 \rightarrow ^3F_4$, $^3F_4$). This process reduces the lifetime of the $^3H_4$ level and consequently the efficiency of the 1450 nm emission.

Energy transfer processes such as cross-relaxation are usually described in terms of three limiting cases: (i) direct relaxation, (ii) fast diffusion, and (iii) diffusion limited relaxation [41]. Fast diffusion is characterized by a simple exponential behavior in the fluorescence

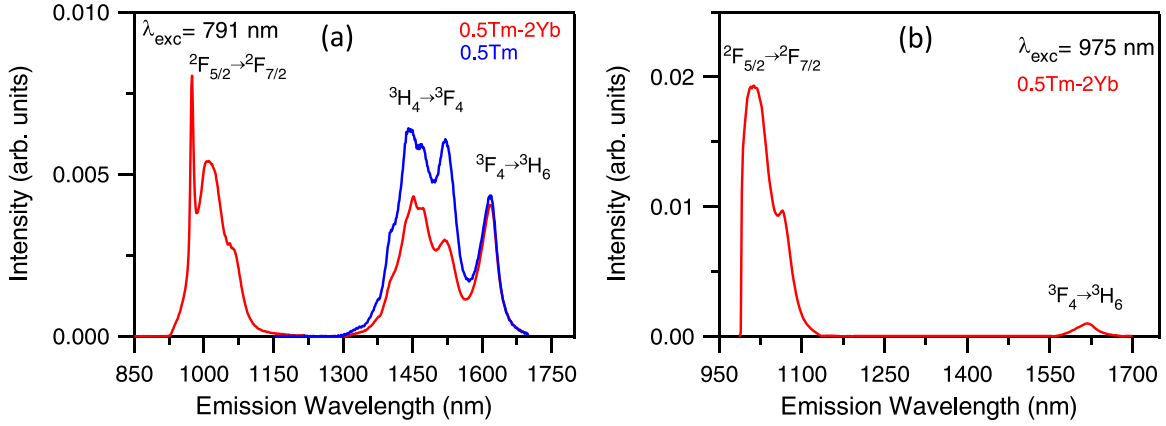


**Fig. 11.** Room temperature emission spectra for glass-ceramic (GC) samples doped with 0.5 mol%. $Tm^{3+}$ (blue line) and codoped with 0.5 mol%. $Tm^{3+}$ – 2 mol%. $Yb^{3+}$(red line), prepared with particle size between 100 and 63 μm, obtained under (a) 791 nm and (b) 975 nm excitations.

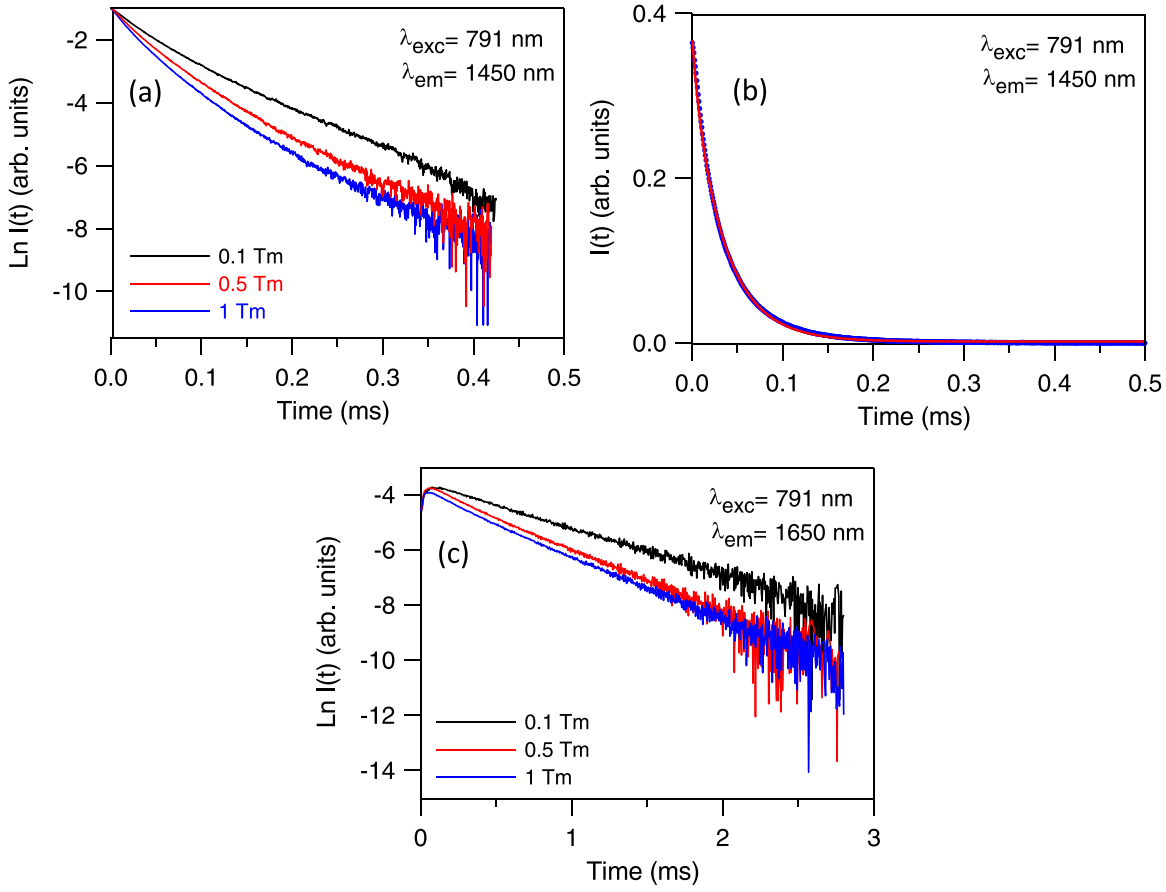


**Fig. 12.** (a) Semilogarithmic plot of the fluorescence decays of the $^3H_4$ level obtained under excitation at 791 nm for the single-doped samples with 0.1, 0.5, and 1 mol% $Tm^{3+}$ prepared with particle size 100–63 μm. (b) Experimental emission decay curve of level $^3H_4$ 1 mol% $Tm^{3+}$ and the calculated fit to Eq. (2) (solid line).(c) Semilogarithmic plot of the fluorescence decays of the $^3F_4$ level obtained under excitation at 791 nm for the single-doped samples with 0.1, 0.5, and 1 mol% $Tm^{3+}$.

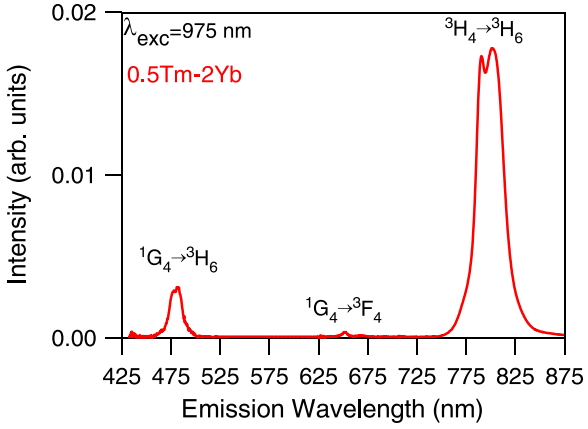


**Fig. 13.** Room temperature UC emission spectrum obtained under 975 nm excitation for the codoped sample with 0.5$Tm^{3+}$ –2$Yb^{3+}$.

decay curve, however decay curves in Fig. 12(a) do not show a simple exponential behavior. The analysis of the decay curves of the $^3H_4$ level shows that energy migration among $Tm^{3+}$ ions affects the energy transfer process. The best agreement between experimental data and theoretical fits is obtained with the expression corresponding to the Burshtein model [42],

$$I(t) = I_0 \exp\left(-\frac{t}{\tau_0} - \gamma\sqrt{t} - Wt\right) \quad (2)$$

where $\tau_0$ is the intrinsic decay time, $\gamma = \frac{4}{3}\pi^{3/2}NC_{DA}^{1/2}$ characterizes the direct energy transfer in the case of dipole-dipole interaction and $W$ represents the migration parameter. In the expression $\gamma$, $N$ is the $Tm^{3+}$ concentration, and $C_{DA}$ is the energy transfer microparameter. Fig. 12(b) shows the fit for the sample doped with 1 mol% $TmF_3$ from which we obtain an intrinsic lifetime of 65 μs, an energy transfer microparameter, of $7.97 \times 10^{-40}$ $cm^6/s$, and a migration parameter of 8440 $s^{-1}$. The critical distance for cross-relaxation, defined as the distance at which the energy transfer probability becomes equal to the intrinsic decay rate of the metastable level can be calculated from, $R_0^6 = \tau_0 C_{DA}$. The critical distance expresses the extent to which the energy transfer can occur between ions. Therefore, the longer the critical distance becomes, the more actively the energy transfer can occur. In this case the value for $R_0$ is 6.1 Å. The observed behavior indicates that the electronic mechanism of energy transfer is a dipole-dipole interaction assisted by energy migration.

In the case of the codoped sample with 0.5 mol%.Tm-2 mol%.Yb, a further reduction of the lifetime of the $^3H_4$ level is observed as compared with the single doped sample due to the Tm-Yb energy transfer. The lifetime is reduced from 43 μs in the single doped sample to 39 μs in the codoped sample.

The decays of the $^3F_4$ level obtained by exciting at 791 nm show an initial rise, due to the lifetime of the $^3H_4$ level, followed by a decay that can be described by a single exponential function to a good approximation. As an example, Fig. 12(c) shows the semilogarithmic plot of the experimental decays of the $^3F_4$ level for the single doped samples with 0.1, 0.5, and 1 mol%. of $TmF_3$. The lifetimes decrease from 682 μs to 370 μs as concentration increases from 0.1 to 1 mol%. of $TmF_3$. In this case, the $^3F_4$ level is the first excited state and

therefore the quenching of luminescence when ion concentration increases can not be due to cross-relaxation between various excited states and it has been mainly considered as due to diffusion towards unidentified impurities or another type of self-generated quenching centers [43]. In the case of fast diffusion, the transfer takes place so quickly that transfer times are averaged out and the system shows an exponential decay as is experimentally observed [44].

Up-conversion (UC) emission has been observed in the codoped sample with 0.5 % Tm-2% Yb after 975 nm excitation of $Yb^{3+}$ ions. The UC emission from $Tm^{3+}$ ions in the wavelength range of 425–825 nm is shown in Fig. 13. The spectrum shows the $^3H_4 \rightarrow {}^3H_6$ transition at around 800 nm together with the blue emission at 480 nm corresponding to the $^1G_4 \rightarrow {}^3H_6$ transition and a weak red emission ($^1G_4 \rightarrow {}^3F_4$) at around 651 nm. The most intense emission was the NIR emission at 800 nm. No UC emission was observed in the single doped samples.

The possible upconversion mechanisms for the UC emissions can be discussed based on the energy level of $Tm^{3+}$ and $Yb^{3+}$ presented in Fig. 14. After 975 nm excitation, the $Yb^{3+}$ ions at the ground state are excited to the $^2F_{5/2}$ state by ground state absorption and then transfer the energy to $Tm^{3+}$ ions following the mechanism $^2F_{5/2} \rightarrow {}^2F_{7/2}$ ($Yb^{3+}$):$^3H_6 \rightarrow {}^3H_5$ ($Tm^{3+}$) (ET1). The $^3H_5$ ($Tm^{3+}$) level populates the $^3F_4$ ($Tm^{3+}$) state by nonradiative relaxation. The second energy transfer process can occur through the mechanism $^2F_{5/2} \rightarrow {}^2F_{7/2}$ ($Yb^{3+}$):$^3F_4 \rightarrow {}^3F_{2,3}$ ($Tm^{3+}$) (ET2). Then multiphonon relaxation from level $^3F_{2,3}$ populates the $^3H_4$ state. From this level a third energy transfer process, $^2F_{5/2} \rightarrow {}^2F_{7/2}$ ($Yb^{3+}$):$^3H_4 \rightarrow {}^1G_4$ ($Tm^{3+}$) (ET3), populates the $^1G_4$ state [45]. According with these mechanisms, the $^3H_4$ ($Tm^{3+}$) state is populated by a two-photon process whereas three-photons are needed to populate the $^1G_4$ ($Tm^{3+}$) state.

The UC emission intensity is related to the pump power excitation by the expression $I_{em} \propto (P_{pump})^n$ where n is the number of photons involved in the process. To obtain information about the processes involved in the UC emission after 975 nm excitation, the UC blue and NIR (800 mm) emissions have been obtained at different pump power densities. The logarithmic plot of the pump power dependence of the UC blue (480 nm) and NIR (800 nm) emissions of the codoped sample show straight lines with slopes 2.11 and 1.41 respectively (Fig. 15). According to the energy level diagram the population of $^3H_4$ and $^1G_4$ levels by successive two and three energy transfers respectively gives a quadratic dependence for the NIR emission and cubic dependence for the blue one. However, the slopes in Fig. 15 deviate from the expected values for ET2 and ET3 processes. The reduction of the slope values could be related to the presence of a saturation effect [46,47]. This behavior, observed in other systems, has been attributed to the competition between the decay rate of the intermediate states and the UC rates. When the UC rate exceeds the decay rate from the intermediate excited states, the experimental power dependence is reduced [48].

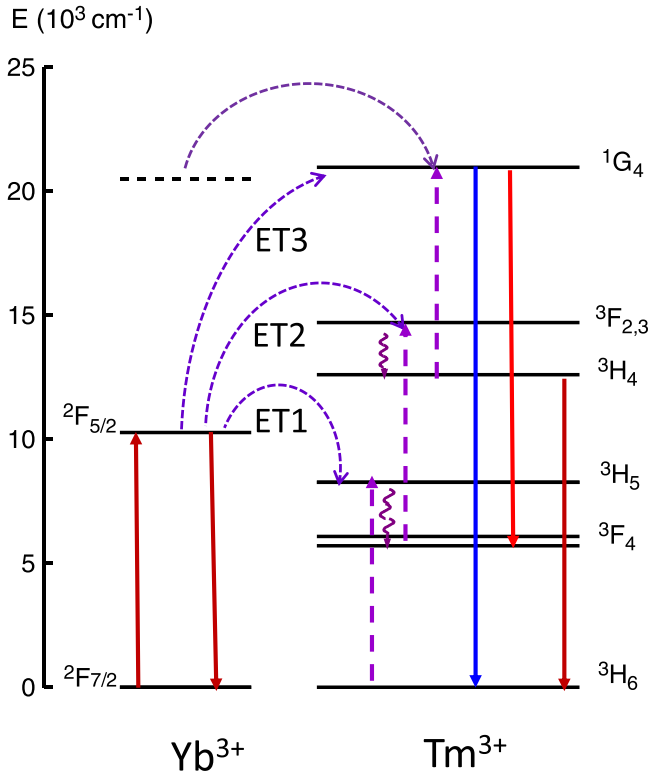


**Fig. 14.** Energy level diagram of $Yb^{3+}$ and $Tm^{3+}$ ions together with the possible energy transfer processes (ET) responsible for the upconverted emissions after excitation at 975 nm ($Yb^{3+}$).

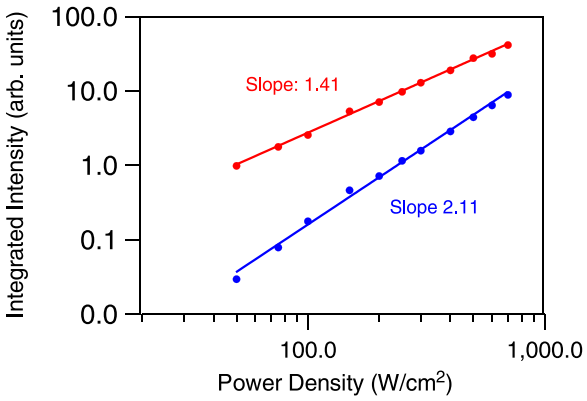


**Fig. 15.** Logarithmic plot of the pump power dependence of the blue ($^1G_4 \rightarrow {}^3H_6$) and NIR ($^3H_4 \rightarrow {}^3H_6$) integrated emission intensities for the codoped GC sample with 0.5Tm–2Yb.

Another possibility to explain the pump power dependence of the UC luminescence is a direct energy transfer from $Yb^{3+}$ ions to the $^3H_4$ level of $Tm^{3+}$ followed by the population of the $^1G_4$ level by another NIR photon. However, we can disregard this process since, as shown in Fig. 11(b), after 975 nm excitation there is not emission from level $^3H_4$.

There is another two-photon mechanism to populate the $^1G_4$ level, proposed by Feofilov and Ovsyankin [49], in which two excited $Yb^{3+}$ ions in the $^2F_{5/2}$ state transfer their energy to a $Tm^{3+}$ ion in the $^3H_6$ ground state by a cooperative sensitization process (Fig. 14). Since the energy of two excited $Yb^{3+}$ ions is almost resonant with $^1G_4$ level, the $Tm^{3+}$ ion is excited from the ground state to the $^1G_4$ emitting level. Based on the pump power dependence of the UC blue emission this process could be responsible for the observed behavior. However, we cannot disregard the presence of successive energy transfer processes ET2 and ET3.

Transparent oxyfluoride GCs containing rare earth doped $NaLaF_4$ nanocrystals have been prepared for the first time using SPS. Following the protocol applied to obtain SPS-GCs based in $KLaF_4$ [14] as crystalline phase, it has been proved that the study of sintering temperatures by means of the heating microscopy technique is efficient when determining the sintering temperature applied in the SPS experiment. It has been confirmed that using larger glass powder particle size, in this case 100-63 µm, leads to a higher transparency of the samples. This may be due to the fact that, in the viscous creep phase, the carbon diffusion in the sample is more difficult. The use of Pt protective films has been confirmed to be useful to reduce C contamination in the samples.

Additionally, $KLaF_4$ crystallization has been achieved in relatively short times, 20 min, compared to the traditional heat treatment method where the times are usually more than 10 h. For this particular phase, the heat treatment times used were in the range of

25–90 h [32]. So, the improvement in terms of treatment time is evident for this particular phase.

Regarding the glass-ceramics optical properties, the NIR and up-conversion emission spectra have demonstrated the effective energy transfer between $Yb^{3+}$ and $Tm^{3+}$ ions. Moreover, the concentration quenching mechanisms of the NIR emissions of $Tm^{3+}$ have been properly analysed from the experimental decays. Future work will continue to totally avoid carbon contamination in order to achieve increasingly transparent materials.

## 4. Conclusions

Transparent oxyfluoride glass-ceramics with $NaLaF_4$ crystalline phase doped with $Tm^{3+}$ and co-doped with $Yb^{3+}$ ions have been successfully produced by the SPS method. This has been possible thanks to the optimization of the SPS process parameters, such as glass powder particle size, temperature, pressure and holding time; permitting to identify of the optimum conditions set as: larger particles sizes (100-63 µm), temperature of 610 °C, pressure of 22 MPa, and time of 20 min.

The presence of β-$NaLaF_4$ nanocrystals with size between 13 and 22 nm have been shown by structural characterization of the GCs doped with 0.1–1.0 mol%. of $TmF_3$. The samples doped with 2.0 mol%. of $TmF_3$ and 0.5 mol%. of $TmF_3$ co-doped with 2.0 mol%. of $YbF_3$ show another crystalline phase, together with β-$NaLaF_4$, corresponding to α- $NaLaF_4$. For these samples, crystal sizes for the beta phase were between 14 and 34 nm.

The $^3H_4 \rightarrow {}^3F_4$ and $^3F_4 \rightarrow {}^3H_6$ emissions have been investigated for different $Tm^{3+}$ concentrations. The non-exponential character of the decay from the $^3H_4$ level, together with the shortening of the life-times with increasing concentration, indicate the presence of cross-relaxation processes between $Tm^{3+}$ ions. The analysis of the decay curves indicates that cross-relaxation occurs via dipole-dipole coupling assisted by energy migration. The concentration quenching of the lifetimes from the $^3F_4$ state can be attributed to fast diffusion towards quenching centers.

Energy transfer between $Yb^{3+}$ and $Tm^{3+}$ ions is confirmed by the NIR and UC emissions after $Yb^{3+}$ excitation at 975 nm. Evidence of back transfer from $Tm^{3+}$ to $Yb^{3+}$ is also provided from the presence of $Yb^{3+}$ emission after near-infrared excitation of $Tm^{3+}$ ions at 791 nm. Blue, red, and NIR upconverted emissions are only observed in $Tm^{3+}$-$Yb^{3+}$ codoped sample after 975 nm excitation, thus confirming the effective energy transfer between $Yb^{3+}$ and $Tm^{3+}$ ions. These up-converted emissions, from $^1G_4$ and $^3H_4$ levels, occur as a consequence of the long lifetime of the first $^3F_4$ excited level.

## CRediT authorship contribution statement

**M. Sedano:** Investigation, Writing – original draft. **S. Babu:** Investigation, Writing – original draft. **R. Balda:** Funding acquisition, Conceptualization, Investigation, Supervision, Writing – review & editing. **J. Fernández:** Conceptualization, Supervision, Writing – review & editing. **A. Durán:** Supervision, Writing – review & editing, Funding acquisition. **M.J. Pascual:** Conceptualization, Methodology, Supervision, Writing – review & editing, Funding acquisition.

## Data availability

Data will be made available on request.

## Declaration of Competing Interest

The authors declare that they have no known competing financial interests or personal relationships that could have appeared to influence the work reported in this paper.

## Acknowledgments

Funding from MICINN under project PID2020–115419 GB-C-21/C-22/AEI/10.13039/501100011033 is acknowledged. This paper is part of the dissemination activities of project FunGlass. This project has received funding from the European Union´s Horizon 2020 research and innovation program under grant agreement No 739566.

## References

[1] Y. Deng, C. Niu, Up-conversion luminescence properties of $Er^{3+}$ /$Yb^{3+}$ co-doped oxyfluoride glass ceramic, J. Lumin. 209 (2019) 39–44, https://doi.org/10.1016/j.jlumin.2018.12.052
[2] M.J. Dejneka, The luminescence and structure of novel transparent oxyfluoride glass-ceramics, J. Alloy. Compd. 239 (1996) 149–155, https://doi.org/10.1016/S0022-3093(98)00731-5
[3] P.P. Fedorov, A.A. Luginina, A.I. Popov, Transparent oxyfluoride glass ceramics, J. Fluor Chem. 172 (2015) 22–50, https://doi.org/10.1016/j.fluchem.2015.01.009
[4] A. De Pablos-Martín, A. Durán, M.J. Pascual, Nanocrystallisation in oxyfluoride systems: mechanisms of crystallisation and photonic properties, Int. Mater. Rev. 57 (2012) 165–186, https://doi.org/10.1179/1743280411Y.0000000004
[5] X. Liu, J. Zhou, S. Zhou, Y. Yue, J. Qiu, Transparent glass-ceramics functionalized by dispersed crystals, Prog. Mater. Sci. 97 (2018) 38–96, https://doi.org/10.1016/j.pmatsci.2018.02.006
[6] A. Herrmann, M. Tylkowski, C. Bocker, C. Rüssel, Cubic and hexagonal $NaGdF_4$ crystals precipitated from an aluminosilicate glass: preparation and luminescence properties, Chem. Mater. 25 (2013) 2878–2884, https://doi.org/10.1021/cm401454y
[7] G. Gorni, R. Balda, J. Fernández, L. Pascual, A. Durán, M.J. Pascual, Effect of the heat treatment on the spectroscopic properties of $Er^{3+}$ -$Yb^{3+}$ -doped transparent oxyfluoride nano-glass-ceramics, J. Lumin 193 (2018) 51–60, https://doi.org/10.1016/j.jlumin.2017.05.063
[8] H. Lee, S.H. Lee, Y.G. Choi, W. Bin Im, W.J. Chung, $Eu^{2+}$ and $Mn^{2+}$ co-doped oxyfluoride glass ceramic for white color conversion of 400 nm UV-LED, J. Lumin 222 (2020) 117156, https://doi.org/10.1016/j.jlumin.2020.117156
[9] G.H. Beall, D.A. Duke, Transparent glass-ceramics, J. Mater. Sci. 4 (1969) 340–352, https://doi.org/10.1007/BF00550404
[10] C. Rüssel, Nanocrystallization of $CaF_2$ from $Na_2O/K_2O/CaO/CaF_2/Al_2O_3/SiO_2$ glasses, Chem. Mater. 17 (2005) 5843–5847, https://doi.org/10.1021/cm051430x
[11] S. Cui, C. Boussard-Plédel, L. Calvez, F. Rojas, K. Chen, H. Ning, M.J. Reece, T. Guizouarn, B. Bureau, Comprehensive study of tellurium based glass ceramics for thermoelectric application, Adv. Appl. Ceram. 114 (2015) S42–S47, https://doi.org/10.1179/1743676115Y.0000000054
[12] M. Hubert, G. Delaizir, J. Monnier, C. Godart, H.-L. Ma, X.-H. Zhang, L. Calvez, An innovative approach to develop highly performant chalcogenide glasses and glass-ceramics transparent in the infrared range, Opt. Express 19 (2011) 23513, https://doi.org/10.1364/oe.19.023513
[13] P. Huang, P. Luo, B. Zhou, L. Wang, W. Jiang, Preparation and luminescence of transparent silica glass-ceramics containing $LaF^3$:$Eu^{3+}$ nanocrystals, Mater. Lett. 271 (2020) 127764, https://doi.org/10.1016/j.matlet.2020.127764
[14] S. Babu, R. Balda, J. Fernández, M. Sedano, G. Gorni, A.A. Cabral, D. Galusek, A. Durán, M.J. Pascual, $KLaF_4$:$Nd^{3+}$ doped transparent glass-ceramics processed by spark plasma sintering, J. Non Cryst. Solids 578 (2022), https://doi.org/10.1016/j.jnoncrysol.2021.121289
[15] G. Delaizir, M. Dollé, P. Rozier, X.H. Zhang, Spark plasma sintering: An easy way to make infrared transparent glass-ceramics, J. Am. Ceram. Soc. 93 (2010) 2495–2498, https://doi.org/10.1111/j.1551-2916.2010.03830.x
[16] A. Öchsner, G.E. Murch, M.J.S. de Lemos, Ralf Riedel (Editor), I-Wei Chen (Editor) - Ceramics Science and Technology, Synthesis and Processing (volume 3) (2011, Wiley-VCH), 2011.
[17] M. Tokita, Spark Plasma Sintering (SPS) Method, Systems, and Applications, second ed., Elsevier Inc, 2013, https://doi.org/10.1016/B978-0-12-385469-8.00060-5
[18] F. Al Mansour, N. Karpukhina, S. Grasso, R.M. Wilson, M.J. Reece, M.J. Cattell, The effect of spark plasma sintering on lithium disilicate glass-ceramics, Dent. Mater. 31 (2015) e226–e235, https://doi.org/10.1016/j.dental.2015.07.001
[19] B. Singarapu, D. Galusek, A. Durán, M.J. Pascual, Glass-ceramics processed by spark plasma sintering (SPS) for optical applications, Appl. Sci. 10 (2020) 1–21, https://doi.org/10.3390/APP10082791
[20] A. De Pablos-Martín, M.A. García, A. Muñoz-Noval, G.R. Castro, M.J. Pascual, A. Durán, Analysis of the distribution of $Tm^{3+}$ ions in $LaF_3$ containing transparent glass-ceramics through X-ray absorption spectroscopy, J. Non Cryst. Solids 384 (2014) 83–87, https://doi.org/10.1016/j.jnoncrysol.2013.07.021
[21] G. Gorni, A. Cosci, S. Pelli, L. Pascual, A. Durán, M.J. Pascual, Transparent oxyfluoride nano-glass ceramics doped with $Pr^{3+}$ and $Pr^{3+}$ -$Yb^{3+}$ for NIR emission, Front. Mater. 3 (2017), https://doi.org/10.3389/fmats.2016.00058
[22] A. De Pablos-Martín, F. Muñoz, G.C. Mather, C. Patzig, S. Bhattacharyya, J.R. Jinschek, T. Höche, A. Durán, M.J. Pascual, $KLaF_4$ nanocrystallisation in oxyfluoride glass-ceramics, CrystEngComm 15 (2013) 10323–10332, https://doi.org/10.1039/c3ce41345d
[23] A.A. Cabral, R. Balda, J. Fernández, G. Gorni, J.J. Velázquez, L. Pascual, A. Durán, M.J. Pascual, Phase evolution of $KLaF_4$ nanocrystals and their effects on the

photoluminescence of $Nd^{3+}$ doped transparent oxyfluoride glass-ceramics, CrystEngComm 20 (2018) 5760–5771, https://doi.org/10.1039/c8ce00897c
[24] A. Tuomela, V. Pankratov, A. Sarakovskis, G. Doke, L. Grinberga, S. Vielhauer, M. Huttula, Oxygen influence on luminescence properties of rare-earth doped $NaLaF_4$, J. Lumin. 179 (2016) 16–20, https://doi.org/10.1016/j.jlumin.2016.06.021
[25] E. Elsts, G. Krieke, U. Rogulis, K. Smits, A. Zolotarjovs, J. Jansons, A. Sarakovskis, K. Kundzins, Rare earth doped glass–ceramics containing $NaLaF_4$ nanocrystals, Opt. Mater. 59 (2016) 130–135, https://doi.org/10.1016/j.optmat.2016.01.005
[26] Y. Le Wei, X.Y. Liu, X.N. Chi, R.F. Wei, H. Guo, Intense upconversion in novel transparent $NaLuF_4$:$Tb^{3+}$, $Yb^{3+}$ glass-ceramics, J. Alloy. Compd. 578 (2013) 385–388, https://doi.org/10.1016/j.jallcom.2013.06.014
[27] J.J. Velázquez, R. Balda, J. Fernández, G. Gorni, G.C. Mather, L. Pascual, A. Durán, M.J. Pascual, Transparent glass-ceramics of sodium lutetium fluoride co-doped with erbium and ytterbium, J. Non Cryst. Solids 501 (2018) 136–144, https://doi.org/10.1016/j.jnoncrysol.2017.12.051
[28] D. Chen, Z. Wan, Y. Zhou, P. Huang, J. Zhong, M. Ding, W. Xiang, X. Liang, Z. Ji, Bulk glass ceramics containing $Yb^{3+}$/$Er^{3+}$: β-$NaGdF_4$ nanocrystals: phase-separation-controlled crystallization, optical spectroscopy and upconverted temperature sensing behavior, J. Alloy. Compd. 638 (2015) 21–28, https://doi.org/10.1016/j.jallcom.2015.02.170
[29] F. Xin, S. Zhao, L. Huang, D. Deng, G. Jia, H. Wang, S. Xu, Up-conversion luminescence of $Er^{3+}$-doped glass ceramics containing β-$NaGdF_4$ nanocrystals for silicon solar cells, Mater. Lett. 78 (2012) 75–77, https://doi.org/10.1016/j.matlet.2012.03.037
[30] Y. Guo, H. Zeng, B. Yang, G. Chen, J. Chen, L. Sun, $Gd^{3+}$ doping induced enhanced upconversion luminescence in $Er^{3+}$/$Yb^{3+}$ co-doped transparent oxyfluoride glass ceramics containing $NaYF_4$ nanocrystals, Ceram. Int. 44 (2018) 10055–10060, https://doi.org/10.1016/j.ceramint.2018.02.184
[31] D. Rajesh, A.S.S. de Camargo, $Nd^{3+}$ doped new oxyfluoro tellurite glasses and glass ceramics containing $NaYF_4$ nano crystals – 1.06 μm emission analysis, J. Lumin 207 (2019) 469–476, https://doi.org/10.1016/j.jlumin.2018.11.058
[32] A. De Pablos-Martín, G.C. Mather, F. Muñoz, S. Bhattacharyya, T. Höche, J.R. Jinschek, T. Heil, A. Durán, M.J. Pascual, Design of oxy-fluoride glass-ceramics containing $NaLaF_4$ nano-crystals, J. Non Cryst. Solids 356 (2010) 3071–3079, https://doi.org/10.1016/j.jnoncrysol.2010.04.057
[33] A. de Pablos-Martín, M.O. Ramírez, A. Durán, L.E. Bausá, M.J. Pascual, $Tm^{3+}$ doped oxy-fluoride glass-ceramics containing $NaLaF_4$ nano-crystals, Opt. Mater. 33 (2010) 180–185, https://doi.org/10.1016/j.optmat.2010.08.004
[34] A. De Pablos-Martin, C. Patzig, T. Höche, A. Duran, M.J. Pascual, Distribution of thulium in $Tm^{3+}$-doped oxyfluoride glasses and glass-ceramics, CrystEngComm 15 (2013) 6979–6985, https://doi.org/10.1039/c3ce40731d
[35] A. de Pablos-Martín, D. Ristic, S. Bhattacharyya, T. Höche, G.C. Mather, M.O. Ramírez, S. Soria, M. Ferrari, G.C. Righini, L.E. Bausá, A. Durán, M.J. Pascual, Effects of $Tm^{3+}$ additions on the crystallization of $LaF_3$ nanocrystals in oxyfluoride glasses: optical characterization and up-conversion, J. Am. Ceram. Soc. 96 (2013) 447–457, https://doi.org/10.1111/jace.12120
[36] M. Środa, Effect of $Er_2O_3$ on thermal stability of oxyfluoride glass, J. Therm. Anal. Calorim. (2009) 239–243, https://doi.org/10.1007/s10973-009-0257-3
[37] G. Gorni, J.J. Velázquez, G.C. Mather, A. Durán, G. Chen, M. Sundararajan, R. Balda, J. Fernández, M.J. Pascual, Selective excitation in transparent oxyfluoride glass-ceramics doped with $Nd^{3+}$, J. Eur. Ceram. Soc. 37 (2017) 1695–1706, https://doi.org/10.1016/j.jeurceramsoc.2016.11.014
[38] A. Bertrand, J. Carreaud, G. Delaizir, J.R. Duclère, M. Colas, J. Cornette, M. Vandenhende, V. Couderc, P. Thomas, A comprehensive study of the carbon contamination in tellurite glasses and glass-ceramics sintered by spark plasma sintering (SPS), J. Am. Ceram. Soc. 97 (2014) 163–172, https://doi.org/10.1111/jace.12657
[39] Y. Peng, J. Zhong, X. Li, J. Chen, J. Zhao, X. Qiao, D. Chen, Controllable competitive nanocrystallization of $La^{3+}$-based fluorides in aluminosilicate glasses and optical spectroscopy, J. Eur. Ceram. Soc. 39 (2019) 1420–1427, https://doi.org/10.1016/j.jeurceramsoc.2018.12.036
[40] J.S. Wang, E.M. Vogel, E. Snitzer, Tellurite glass: a new candidate for fiber devices, Opt. Mater. 3 (1994) 187–203, https://doi.org/10.1016/0925-3467(94)90004-3
[41] M.J. Weber, Luminescence decay by energy migration and transfer: observation of diffusion-limited relaxation, Phys. Rev. B 4 (1971) 2932–2939.
[42] A.I. Burshtein, Hopping mechanism of energy transfer, Sov. JETP Phys. 35 (1972) 882–885.
[43] F. Auzel, A fundamental self-generated quenching center for lanthanide-doped high-purity solids, J. Lumin. 100 (2002) 125–130, https://doi.org/10.1016/S0022-2313(02)00457-X
[44] M.J. Weber, Luminescence decay by energy migration and transfer: observation of diffusion-limited relaxation, Phys. Rev. B 4 (1971) 2932–2939, https://doi.org/10.1103/physrevb.4.2932
[45] M. Quintanilla, N.O. Núñez, E. Cantelar, M. Ocaña, F. Cussó, Energy transfer efficiency in $YF_3$ nanocrystals: quantifying the $Yb^{3+}$ to $Tm^{3+}$ infrared dynamics, J. Appl. Phys. 113 (2013) 2–8, https://doi.org/10.1063/1.4803540
[46] M. Pollnau, D.R. Gamelin, S.R. Lüthi, H.U. Güdel, Power dependence of upconversion luminescence in lanthanide and transition-metal-ion systems, Phys. Rev. B 61 (2000) 3337–3346, https://doi.org/10.1103/PhysRevB.61.3337
[47] K. Halubek-Gluchowska, D. Szymański, T.N.L. Tran, M. Ferrari, A. Lukowiak, Upconversion luminescence of silica–calcia nanoparticles co-doped with $Tm^{3+}$ and $Yb^{3+}$ ions, Materials 14 (2021) 1–19, https://doi.org/10.3390/ma14040937
[48] J.F. Suyver, A. Aebischer, S. García-Revilla, P. Gerner, H.U. Güdel, Anomalous power dependence of sensitized upconversion luminescence, Phys. Rev. B Condens Matter Mater. Phys. 71 (2005) 1–9, https://doi.org/10.1103/PhysRevB.71.125123
[49] P.P. Feofilov, V.V. Ovsyankin, Cooperative luminescence of solids, Appl. Opt. 6 (1967) 1828–1833, https://doi.org/10.1364/ao.6.001828